Robust Direct Model Predictive Control with Reduced Computational Effort for Medium-Voltage Grid-Connected Converters with LCL Filters

Andrei Tregubov*, Petros Karamanakos*, Ludovico Ortombina†
*Faculty of Information Technology and Communication Sciences, Tampere University
33101 Tampere, Finland
†Department of Industrial Engineering, University of Padua
35122 Padua, Italy

E-Mail: andrei.tregubov@tuni.fi, p.karamanakos@ieee.org, ludovico.ortombina@unipd.it

***Index Terms*—Grid-connected converter, model predictive control, estimation technique, medium-voltage converter, 3-level NPC.**

***Abstract*—The performance benefits of long-horizon direct model predictive control (MPC) methods become more evident when high-order systems are considered. However, such applications pose a challenge implementation-wise as the increased size of the system model and adoption of long horizons can significantly increase the computational requirements of direct MPC. In addition, variations in the system parameters may deteriorate the controller operation. The presented method allows to harvest the performance benefits of long-horizon direct MPC with modest computational effort. This is achieved by adopting a split horizon formulation that enables the fulfillment of two tasks, namely, the prediction of the system behavior and evaluation of the candidate switch positions with marginal computational overhead. Moreover, to enhance the controller robustness to parameter variations, a simple estimator of the grid reactance is introduced. The effectiveness of the proposed approach is verified with a medium-voltage three-level neutral-point-clamped converter connected to the grid via an LCL filter.**

I. Introduction

For the integration of high-power and high-performance variable speed drives into the electrical grid, medium-voltage (MV) converters are a viable choice. These are often equipped with LCL filters to dampen the harmonic components that are generated by the switching behavior of power electronics. However, such applications constitute high-order systems that pose a challenge for conventional control strategies because of their typically single-input single-output nature. Notably, a promising alternative to the established linear control techniques, i.e., model predictive control (MPC), continues to gain popularity in the academia also because of its ability to handle multiple-input multiple-output (MIMO) systems [1]. That is, for the systems of interest, MPC is able to control the converter and the grid currents along with the capacitor voltage.

Besides the MIMO nature, it has been shown that MPC achieves superior performance and guarantees stability when long prediction horizons are employed [2]. However, doing this in real time, especially for finite control set MPC (FCS-MPC) methods, where control actions are applied directly to a converter without a modulator stage, is a non-trivial task. This is due to the size of the underlying optimization problem that increases exponentially with the number of the prediction horizon steps [3]. Existing solutions offer sophisticated algorithms—e.g., the sphere decoder algorithm (SDA)—that manage to find the optimal switching signals in a significantly reduced (on average) time. The said method, however, is limited to linear, time-invariant systems [4], [5]. Adoption of non-trivial prediction horizons is another approach in the direction towards decreasing the computational complexity [6], [7]. Nevertheless, keeping the calculation effort at levels suitable for a real-time implementation while gaining advantages associated with long horizons remains a challenge for MPC [1].

As its name suggests, MPC is a technique based on the system model. Thus, the accuracy of the latter plays an important role in the controller performance. Despite the fact that the models of power electronic systems are typically accurate, their parameters do not always remain constant. For example, inductor and capacitor values in LCL filters deviate in time but at a very slow rate,

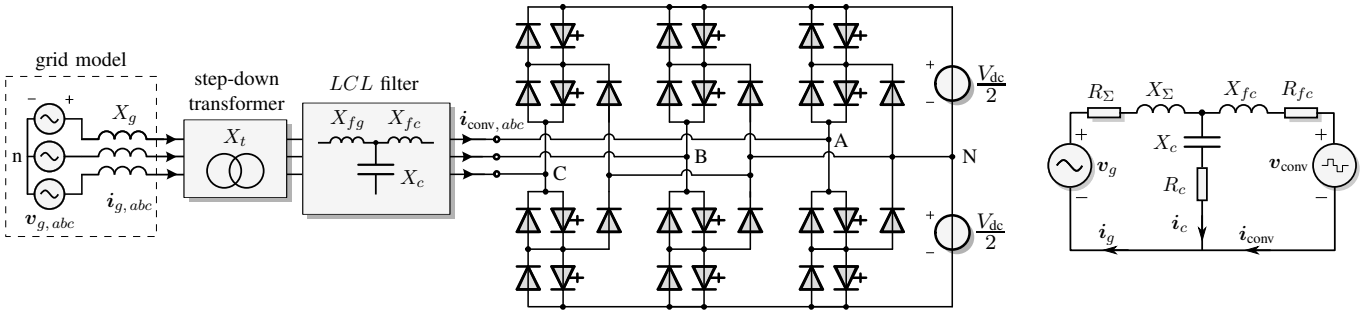

Fig. 1. Grid-connected three-level NPC converter with the LCL filter on the left and its equivalent circuit in the $\alpha\beta$-plane on the right.

mainly due to aging phenomena [8]. On the contrary, the grid reactance varies depending on operating conditions, and its actual value is hard to predict. Thus, its real-time estimation improves the accuracy of the prediction model and results in better control actions.

On a high level, estimation techniques for the grid reactance can be divided into passive, active, and quasi-passive. These methods either utilize information acquired during transients, or by injecting perturbations, or by a combination of both [9]. For example, to obtain the grid reactance value with passive online techniques, a Kalman filter is typically used [10]–[12]. Such methods may require a trial-and-error tuning procedure [10], or a calculation can be performed only in steady state [12], or during a specific part of the fundamental period [11]. Alternatively, a non-invasive recursive least squares (RLS) algorithm can monitor the grid impedance. However, it requires a change between at least two distinct converter operating points to have a reliable estimation result [13]. Another work uses an RLS algorithm to take advantage of the switching noise, which is—typically for direct control methods—spread over a wide frequency range, to obtain the grid reactance [14]. However, in order to run the estimation algorithm in conjunction with the long-horizon MPC, its complexity has to be as low as possible to limit the calculation load of the control task. This point is often not considered in other works.

Given the above, this paper proposes a long-horizon FCS-MPC method for MV grid-connected three-level neutral-point-clamped (NPC) converters with LCL filters that has a modest computational burden and is robust to grid reactance variations. The latter is accomplished by devising a simple grid-side reactance estimator. The former is met by formulating the objective function in a way such that only a limited number of candidate solutions is considered for the optimization problem, thus effectively decreasing its computational demands. With the said approach, an improved steady-state performance is achieved with a long-horizon FCS-MPC scheme that is computationally light and, thus, suitable for real-time implementation.

TABLE I
MV SYSTEM RATED VALUES AND PARAMETERS

Parameter	Value
Rated voltage V_R	3300 V
Rated current I_R	1575 A
Apparent power S_R	9 MVA
Grid frequency f_g	50 Hz
Dc-link voltage V_{dc}	5.2 kV
Grid inductance L_g	0.403 mH
Grid resistance R_g	12.6 mΩ
Grid-side filter inductance L_{fg}	0.282 mH
Grid-side filter resistance R_{fg}	0.484 mΩ
Converter-side filter inductance L_{fc}	0.452 mH
Converter-side filter resistance R_{fc}	0.484 mΩ
Filter capacitance C	884.9 μF
Filter resistance R_c	0.484 mΩ
Transformer inductance L_t	0.346 mH
Transformer resistance R_t	9.1 mΩ

II. Modeling

The considered case study is the three-level NPC grid-tied converter with the LCL filter shown in Fig. 1 with parameters and rated values in Table I. The work adopts the $\alpha\beta$ reference frame. For simplicity the corresponding subscript for variables in $\alpha\beta$-frame is dropped in the text and figures, whereas the subscript for variables in the abc-plane is kept. Furthermore, all SI variables are normalized based on the rated values of the secondary side of the step-down transformer, and the per unit (p.u.) system is adopted.

Several simplifications are assumed for the chosen case study. Specifically, the grid source is modeled with an ideal and symmetrical voltage $\boldsymbol{v}_{g,abc}$. Likewise, the grid resistance R_g and the grid reactance X_g are equal for all phases and model the transmission lines. The converter dc-link voltage V_{dc} is assumed to be constant, and the neutral point potential v_n is fixed to zero. The

transformer is approximated with its leakage reactance X_t and resistance R_t.

The converter voltage $\boldsymbol{v}_{\text{conv}}$ is derived from the converter three-phase switch position $\boldsymbol{u}_{abc}$ using the reduced Clarke transformation matrix $\boldsymbol{K}$ [2, Chapter 2.1]:

$$\boldsymbol{v}_{\text{conv}} = \frac{V_{\text{dc}}}{2}\boldsymbol{K}\boldsymbol{u}_{abc}, \tag{1}$$

with $\boldsymbol{u}_{abc} = [u_a \ u_b \ u_c]^T$, where $u_x \in \mathcal{U} = \{-1, 0, 1\}$, $x \in \{a, b, c\}$ is the single-phase switch position.

The conventional direction of the grid $\boldsymbol{i}_g$, converter $\boldsymbol{i}_{\text{conv}}$, and capacitor $\boldsymbol{i}_c$ currents (and correspondingly for the capacitor voltage $\boldsymbol{v}_c$) are shown in Fig. 1. Then by considering (1), and the assumptions above, the dynamics of the system can be described with the continuous-time state-space form

$$\frac{\mathrm{d}\boldsymbol{x}(t)}{\mathrm{d}t} = \mathbf{F}\boldsymbol{x}(t) + \mathbf{G}\boldsymbol{u}_{abc}(t) \tag{2a}$$

$$\boldsymbol{y}(t) = \mathbf{C}\boldsymbol{x}(t), \tag{2b}$$

where the state vector is chosen as $\boldsymbol{x} = [\boldsymbol{i}_{\text{conv}}^T \ \boldsymbol{v}_c^T \ \boldsymbol{i}_g^T \ \boldsymbol{v}_g^T]^T$, the output $\boldsymbol{y} = [\boldsymbol{i}_{\text{conv}}^T \ \boldsymbol{v}_c^T \ \boldsymbol{i}_g^T]^T$, and the control input is $\boldsymbol{u}_{abc}$. The system dynamics is defined by the matrix $\mathbf{F} \in \mathbb{R}^{8\times 8}$

$$\mathbf{F} = \begin{bmatrix} -\frac{(R_{fc}+R_c)}{X_{fc}}\boldsymbol{I}_2 & \frac{1}{X_{fc}}\boldsymbol{I}_2 & \frac{R_c}{X_{fc}}\boldsymbol{I}_2 & \mathbf{0}_{2\times 2} \\ -\frac{1}{X_c}\boldsymbol{I}_2 & \mathbf{0}_2 & \frac{1}{X_c}\boldsymbol{I}_2 & \mathbf{0}_{2\times 2} \\ \frac{R_c}{X_\Sigma}\boldsymbol{I}_2 & -\frac{1}{X_\Sigma}\boldsymbol{I}_2 & -\frac{(R_\Sigma+R_c)}{X_\Sigma}\boldsymbol{I}_2 & \frac{1}{X_\Sigma}\boldsymbol{I}_2 \\ \mathbf{0}_{2\times 2} & \mathbf{0}_{2\times 2} & \mathbf{0}_{2\times 2} & \omega_g\tilde{\boldsymbol{Q}} \end{bmatrix},$$

with $\boldsymbol{I}$, $\mathbf{0}$ and $\tilde{\boldsymbol{Q}} = \left(\begin{smallmatrix} 0 & -1 \\ 1 & 0 \end{smallmatrix}\right)$ being the identity, zero and rotation matrices, respectively. Note that the subscripts in resistances R_x and reactances L_x, $x \in \{fc, fg, c\}$, refer to the converter-side, grid-side and capacitor elements, respectively. Also, the grid-side lumped resistance and reactance are $R_\Sigma = R_{fg} + R_t + R_g$, and $X_\Sigma = X_{fg} + X_t + X_g$, respectively. Furthermore, the input $\boldsymbol{G}$ and output $\boldsymbol{C}$ matrices are

$$\mathbf{G} = -\frac{V_{\text{dc}}}{2X_{fc}}\begin{bmatrix}\boldsymbol{I}_2 & \mathbf{0}_{2\times 6}\end{bmatrix}^T\boldsymbol{K}, \qquad \mathbf{C} = \begin{bmatrix}\boldsymbol{I}_6 & \mathbf{0}_{6\times 2}\end{bmatrix}.$$

As the last step, the prediction model for the FCS-MPC scheme is obtained through discretization of (2) using the forward Euler method with the controller sampling interval T_s:

$$\boldsymbol{x}(k+1) = \mathbf{A}\boldsymbol{x}(k) + \mathbf{B}\boldsymbol{u}_{abc}(k) \tag{3a}$$

$$\boldsymbol{y}(k) = \mathbf{C}\boldsymbol{x}(k), \tag{3b}$$

where $\mathbf{A} = \boldsymbol{I}_8 + \mathbf{F}T_s$, and $\mathbf{B} = \mathbf{G}T_s$ and $k \in \mathbb{N}$ [1].

III. Controller Design

A. Optimization Problem

The controller objective is to manipulate the converter switch position $\boldsymbol{u}_{abc}$ such that the output variables $\boldsymbol{y}$ follow their references $\boldsymbol{y}_{\text{ref}}$, and the system is operated at a low switching frequency f_{sw}. The described approach is translated into the following objective function

$$J = \sum_{\ell=k}^{k+N_p-1} \|\boldsymbol{y}_{\text{err}}(\ell+1)\|_{\boldsymbol{Q}}^2 + \lambda_u \sum_{\ell=k}^{k+N_c-1} \|\Delta\boldsymbol{u}_{abc}(\ell)\|_2^2. \tag{4}$$

The first term in (4) denotes the tracking error $\boldsymbol{y}_{\text{err}} = \boldsymbol{y}_{\text{ref}} - \boldsymbol{y}$, the second one is the control effort $\Delta\boldsymbol{u}_{abc}(\ell) = \boldsymbol{u}_{abc}(\ell) - \boldsymbol{u}_{abc}(\ell-1)$, and $\lambda_u > 0$ sets the trade-off between the two terms, i.e., the tracking of the output references and the switching frequency. In addition, the computed deviations in $\boldsymbol{y}_{\text{err}}$ are weighted with the elements of the diagonal matrix $\boldsymbol{Q}_{6\times 6} \succeq \mathbf{0}$ that set the tracking priority between the controlled variables. Finally, the prediction horizon $N_p \cdot T_s$ defines the time window wherein the system state is predicted, i.e., the output $\boldsymbol{y}(\ell)$ is calculated using the prediction model (3), while the control horizon N_c refers to the number of steps wherein all feasible switch positions $\boldsymbol{u}_{abc}(\ell)$ are evaluated. Based on (4), the following optimization problem is solved

$$\underset{\boldsymbol{U}(k)\,\in\,\mathbb{U}}{\text{minimize}} \ J(k) \tag{5a}$$

$$\text{subject to} \tag{5b}$$

$$\boldsymbol{x}(j+1) = \mathbf{A}\boldsymbol{x}(j) + \mathbf{B}\boldsymbol{u}_{abc}(\ell) \tag{5c}$$

$$\boldsymbol{y}(j+1) = \mathbf{C}\boldsymbol{x}(j+1), \forall j = k, \ldots, k+N_p-1 \tag{5d}$$

$$\|\Delta\boldsymbol{u}_{abc}(\ell)\|_\infty \leq 1, \qquad \forall \ell = k, \ldots, k+N_c-1, \tag{5e}$$

where $\mathbb{U} = \boldsymbol{\mathcal{U}} \times \cdots \times \boldsymbol{\mathcal{U}}$ is the $3N_c$-times Cartesian product of the set $\boldsymbol{\mathcal{U}}$, and represents the feasible input set. By solving (5) the controller concludes to the optimal sequence of switch positions

$$\boldsymbol{U}^*(k) = \left[\boldsymbol{u}_{abc}^{*T}(k) \ \boldsymbol{u}_{abc}^{*T}(k+1) \ \ldots \ \boldsymbol{u}_{abc}^{*T}(k+N_c-1)\right]^T.$$

Typically, (5) is solved using an enumeration strategy, however, the computational complexity of the problem grows exponentially with the size of the optimization vector, i.e., the switching sequence $\boldsymbol{U}(k)$, thus posing challenges for FCS-MPC implementations in real time [1]. As a consequence, many works consider one-step horizon, thus hindering the potential of long-horizon MPC to deliver improved performance and guaranteed stability [3].

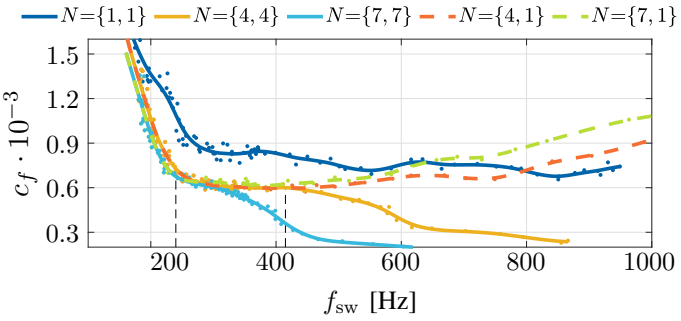

Fig. 2. Performance metric c_f as a function of the switching frequency f_{sw} for horizon combinations $N = \{1,1\}$, $\{4,4\}$, $\{7,7\}$, $\{4,1\}$, and $\{7,1\}$. Individual simulations are indicated by dots, and their trends are approximated with polynomials.

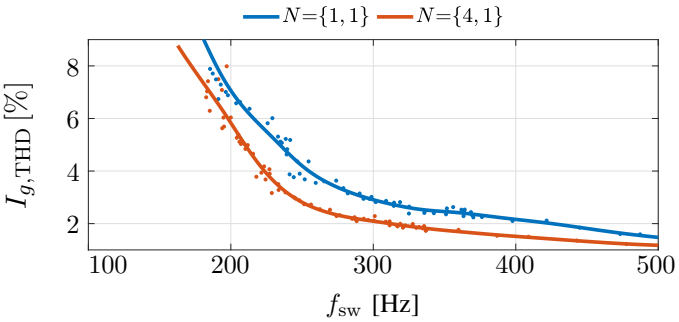

Fig. 3. The trade-off curve between the grid current THD $I_{g,\mathrm{THD}}$ and the switching frequency f_{sw} for FCS-MPC with the horizon combinations $N = \{1,1\}$ and $\{4,1\}$ for $T_s = 50\,\mu$s.

To address the above, the horizon combination $N = \{N_p, N_c\}$ is introduced in (5) with the aim to decrease the size of the optimization problem by keeping the control horizon short $N_c < N_p$. Nonetheless, performance benefits associated with long prediction horizons N_p can be fully gained, since—according to the receding horizon policy [3]—only $\boldsymbol{u}^*_{abc}(k)$ is applied to the converter. Therefore, keeping the last calculated $\boldsymbol{u}^*_{abc}(k+N_c-1)$ for the remaining $N_p - N_c$ steps does not deteriorate the system performance. The favorable controller behavior, however, has to be ensured, as it is directly affected by the prediction window $N_p \cdot T_s$, what is demonstrated in the following subsection.

B. Assessment of the Objective Function

The objective function (4) is evaluated for a set of simulations at nominal steady-state operation with unity power factor, i.e., $P_{\mathrm{ref}} = 1$, $Q_{\mathrm{ref}} = 0$. Each simulation has a duration of 20 fundamental periods at a specific f_{sw} between approximately 200 Hz and 1000 Hz. The range of f_{sw} is defined by a corresponding set of λ_u values, while the sampling interval is set to $T_s = 50\,\mu$s. The grid current total harmonic distortion (THD) $I_{g,\mathrm{THD}}$ is recorded for each f_{sw} to calculate the metric $c_f = I_{g,\mathrm{THD}} \cdot f_{\mathrm{sw}}$. Since c_f approximates a hyperbolic trade-off between $I_{g,\mathrm{THD}}$ and f_{sw}, its lower values correspond to a favorable system behavior. The weighting matrix is set to $\boldsymbol{Q} = \mathrm{diag}(1,1,50,50,500,500)$. As can be understood, this way the grid current bears the highest tracking priority, whereas the converter current has the lowest one. This setting affects the grid current spectrum, as will be shown in Section VI.

The said evaluation of the controller design is presented in Fig. 2, where five different horizon combinations are studied. The results show that, as expected, c_f is inversely proportional to N_p, at least for low f_{sw}. For example, the combination $N = \{7,7\}$ clearly outperforms $N = \{4,4\}$, which in turn has lower c_f values than $N = \{1,1\}$. It can be noted that around the system resonance frequency

$$f_{\mathrm{res}} = \frac{\omega_B}{2\pi}\sqrt{\frac{X_{fc}+X_\Sigma}{X_c X_{fc} X_\Sigma}} = 301\,\mathrm{Hz}. \tag{6}$$

the steady-state performance does not exhibit any visible increase in the c_f metric, even though the resistances of the filter do not provide any passive damping due to their small values, as can be deduced from Table I.

As indicated by the vertical dashed lines in Fig. 2, the metric starts to rise at specific frequencies $f_{\mathrm{sw}} = f_{\mathrm{sw}}^{\mathrm{crit}}$ around 420 Hz for the combination $N = \{4,1\}$ and 240 Hz for $N = \{7,1\}$. This is explained by the minimum number of anticipated changes in the switch position when operating below the critical switching frequency $f_{\mathrm{sw}}^{\mathrm{crit}}$. For a three-level converter with 12 semiconductor devices $f_{\mathrm{sw}}^{\mathrm{crit}}$ can be found according to [15]

$$N_p \cdot T_s = (12 f_{\mathrm{sw}}^{\mathrm{crit}})^{-1}, \tag{7}$$

where the right-hand side indicates the average time between two consecutive switching transitions [7]. Then by equating it to the time window $N_p \cdot T_s$, the expression (7) represents the system operation when only one switching transition occurs within the prediction horizon N_p.

Notably, the combination $N = \{4,1\}$ achieves similar steady-state performance as, e.g., the combination $N = \{4,4\}$ in Fig. 2 for $f_{\mathrm{sw}} < 500$ Hz, whereas a real-time implementation of such a long control horizon is hardly possible with the exhaustive search algorithm. Certainly, more sophisticated solvers can be used instead, e.g., SDA [4], [5], thus allowing to deploy a long-horizon FCS-MPC to a hardware with sampling intervals of few μs [16]. In doing so, however, and when system parameter deviations are concerned, updating the prediction model at every sampling interval becomes a

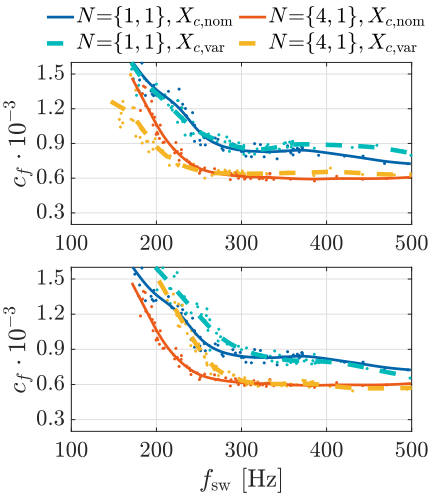

(a) Variations in X_c: Top figure $+20\%$ variation; bottom figure -20% variation

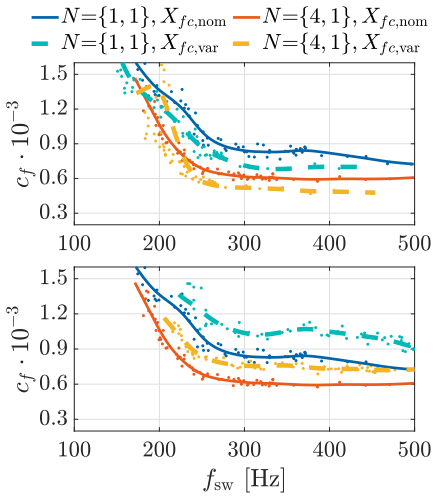

(b) Variations in X_{fc}: Top figure $+20\%$ variation; bottom figure -20% variation

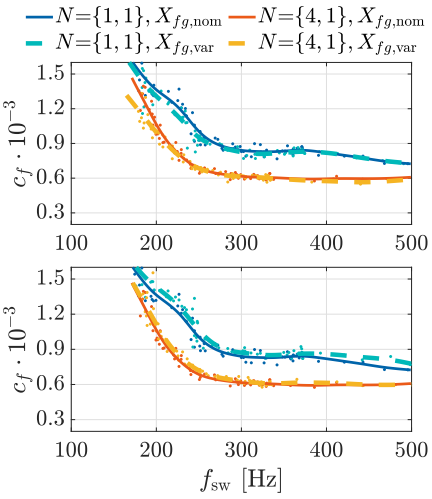

(c) Variations in X_{fg}: Top figure $+20\%$ variation; bottom figure -20% variation

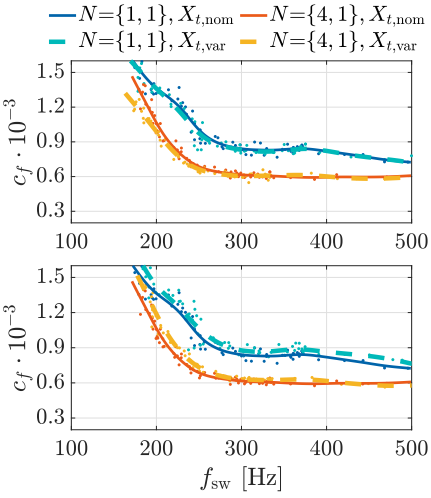

(d) Variations in X_t: Top figure $+20\%$ variation; bottom figure -20% variation

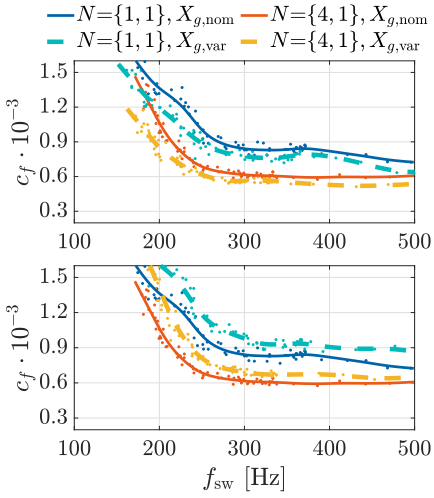

(e) Variations in X_g: Top figure $+20\%$ variation; bottom figure -20% variation

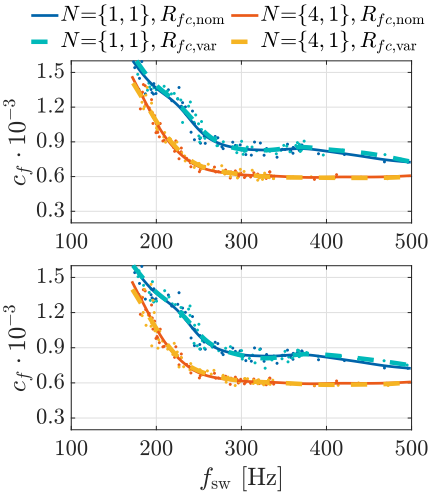

(f) Variations in R_{fc}: Top figure $+50\%$ variation; bottom figure -50% variation

Fig. 4. Simulation results for the performance metric c_f as a function of the switching frequency f_{sw} for horizon combinations $N{=}\{1, 1\}$ and $\{4, 1\}$. c_f resulting from the nominal parameters is shown with solid lines, while c_f that corresponds to cases with parameter variations is shown with dashed lines.

time demanding task, as it involves, inter alia, matrix inversions in real time [2, Chapter 5.2]. Thus, depending on the application and the hardware, implementation of the exhaustive search algorithm with a split horizon may be a feasible approach.

To conclude the discussion above, Fig. 3 shows $I_{g,\text{THD}}$ for the horizon combinations $\{1, 1\}$ and $\{4, 1\}$, which are chosen for further analysis. It is seen that a longer prediction horizon offers smaller current distortions by 1.5 to 2 % in the low-frequency range where MV applications typically operate. Such an improvement comes at a marginal computational cost, since the size of the optimization problem for $N{=}\{4, 1\}$ is similar to that of one-step FCS-MPC.

IV. Robustness Analysis

The proposed direct MPC strategy requires an accurate model to predict its state over the prediction horizon using (3). In cases where the system parameters change over time, the controller behavior may deteriorate. To illustrate such a dependency, a robustness analysis is conducted in this section by introducing variations into the prediction-model parameters and recording the metric c_f over the same range of f_{sw} as in the previous section. For completeness, the results in Fig. 4 consider variations in all the system parameters. While the maximum deviations in the filter and transformer elements are set to $\pm 20\%$, the grid reactance X_g has mismatches of $\pm 50\%$.

As can be seen in Fig. 4, the controller performance

is mostly sensitive to mismatches in the filter elements, with the converter-side reactance variations being the most prominent affecting factor. However, the said components change their values only slightly in practice, and mainly due to a gradual degradation over their lifetime. Therefore, these variations are not considered for an online estimation in conjunction with FCS-MPC.

On the contrary, variations in the grid reactance may lead to suboptimal operation. Fig. 4 shows that when X_g deviates from its nominal value, the controller performance metric is clearly compromised. Naturally, the bigger the grid reactance value is the greater its variations affect the grid-side lumped reactance X_Σ. For the parameters in Table I a mismatch of $50\,\%$ in X_g causes approximately a $20\,\%$ change in X_Σ.

Finally, resistance deviations have a negligible effect on the performance mostly due to their low values. Note that the results are shown only for the mismatches in the converter-side resistance R_{fc}.

V. Estimator Derivation

The estimator design is based on the equivalent circuit in Fig. 1 and the assumption of an ideal grid voltage. Then, with the differential equation for the system dynamics

$$\widehat{X}_\Sigma \frac{\mathrm{d}\boldsymbol{i}_g}{\mathrm{d}t} + X_{fc}\frac{\mathrm{d}\boldsymbol{i}_{\text{conv}}}{\mathrm{d}t} = \boldsymbol{v}_g(t) - \boldsymbol{v}_{\text{conv}}(t)\,, \tag{8}$$

the estimated value $\widehat{X}_\Sigma$ can be deduced from

$$\begin{aligned}&\|\boldsymbol{v}_g(k)\|_2^2 - \|\boldsymbol{v}_g(k-1)\|_2^2 = \\ &v_{g,\alpha}^2(k) + v_{g,\beta}^2(k) - v_{g,\alpha}^2(k-1) - v_{g,\beta}^2(k-1) = 0\end{aligned} \tag{9}$$

that holds true as long as the amplitude of the grid voltage does not change between two consecutive discrete time steps, which is typically the case. By discretizing (8) with the forward Euler method, each term of (9) can be calculated as

$$\begin{aligned}v_{g,z}^2(\ell) = (&\widehat{X}_\Sigma \Delta A_{g,z}(\ell+1) + \\ &X_{fc}\Delta A_{\text{conv},z}(\ell+1) + v_{\text{conv},z}(\ell)\,)^2\,,\end{aligned} \tag{10}$$

where

$$\Delta A_{g,z}(\ell+1) = \frac{i_{g,z}(\ell+1) - i_{g,z}(\ell)}{T_s}\,, \tag{11a}$$

$$\Delta A_{\text{conv},z}(\ell+1) = \frac{i_{\text{conv},z}(\ell+1) - i_{\text{conv},z}(\ell)}{T_s} \tag{11b}$$

with $z \in \{\alpha, \beta\}$, and $\ell \in \{k, k-1\}$. For example, for $z = \alpha$ and $\ell = k-1$, $v_{g,\alpha}(k-1)$ is calculated as

$$\begin{aligned}v_{g,\alpha}^2(k-1) = \Bigg(&\widehat{X}_\Sigma \cdot \frac{i_{g,\alpha}(k) - i_{g,\alpha}(k-1)}{T_s} \\ &+ \widehat{X}_{fc} \cdot \frac{i_{\text{conv},\alpha}(k) - i_{\text{conv},\alpha}(k-1)}{T_s} + v_{\text{conv},\alpha}(k-1)\Bigg)^2\,.\end{aligned}$$

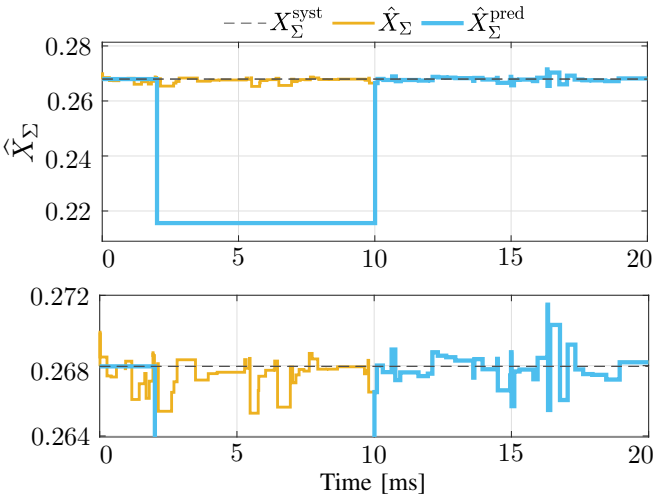

Fig. 5. Simulation results for estimation of the lumped grid-side reactance (up) and its zoomed-in view (down).

With the help of (10) and (11), (9) can be written in the form of the following quadratic equation [17]

$$\widehat{X}_\Sigma^2 A + \widehat{X}_\Sigma B + C = 0\,, \tag{12}$$

where A, B, C are given in the appendix.

After substituting (14) into (12), the grid side lumped reactance is obtained with

$$\widehat{X}_{\Sigma 1,2} = \frac{B}{2A}\left[-1 \pm \sqrt{1 - \frac{4CA}{B^2}}\right]\,, \tag{13}$$

where one of the roots is kept. The choosing criterion for the latter is described in detail in [15].

The calculation accuracy of the lumped grid-side reactance is shown is Fig. 5, wherein deviations of the estimated value $\widehat{X}_\Sigma$ lie within the $\pm 1\,\%$ interval from the nominal value $X_\Sigma^{\text{syst}} = 0.268\,\text{p.u.}$ To demonstrate the estimator operation, FCS-MPC starts to control the system based on the nominal system reactance $X_\Sigma^{\text{pred}} = X_\Sigma^{\text{syst}}$, shown with the dashed line in Fig. 5. Following, the grid reactance X_g in the prediction model is reduced by $50\,\%$ at $2\,\text{ms}$, resulting in a lumped grid-side reactance decreased by $\approx 20\,\%$, yielding $X_\Sigma^{\text{pred}} \approx 0.21\,\text{p.u.}$ Meanwhile, the estimator calculates $\widehat{X}_\Sigma$ in parallel to the control scheme up to $t = 10\,\text{ms}$ when the direct MPC starts to use the estimated values for updating the prediction model, i.e., $X_\Sigma^{\text{pred}} = \widehat{X}_\Sigma$.

VI. Estimator Performance Evaluation

In this section, the operation of the proposed FCS-MPC scheme with the estimation algorithm is verified in the time domain. The simulation results for steady-state operation are shown in Fig. 6 with the settings mentioned

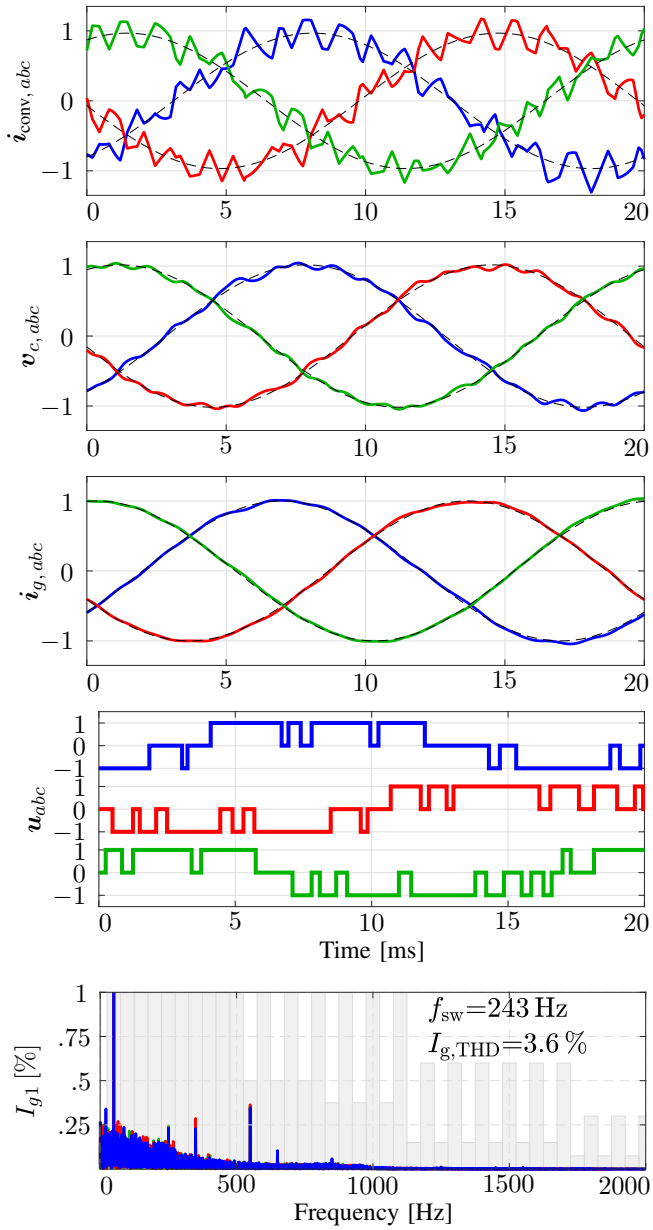

Fig. 6. Simulation results at steady-state operation with the proposed FCS-MPC for $N = \{4, 1\}$ when a mismatch of -50% is introduced in the grid reactance X_g and the estimator is active. The gray bars in the spectrum indicate grid current distortion limits set by [18].

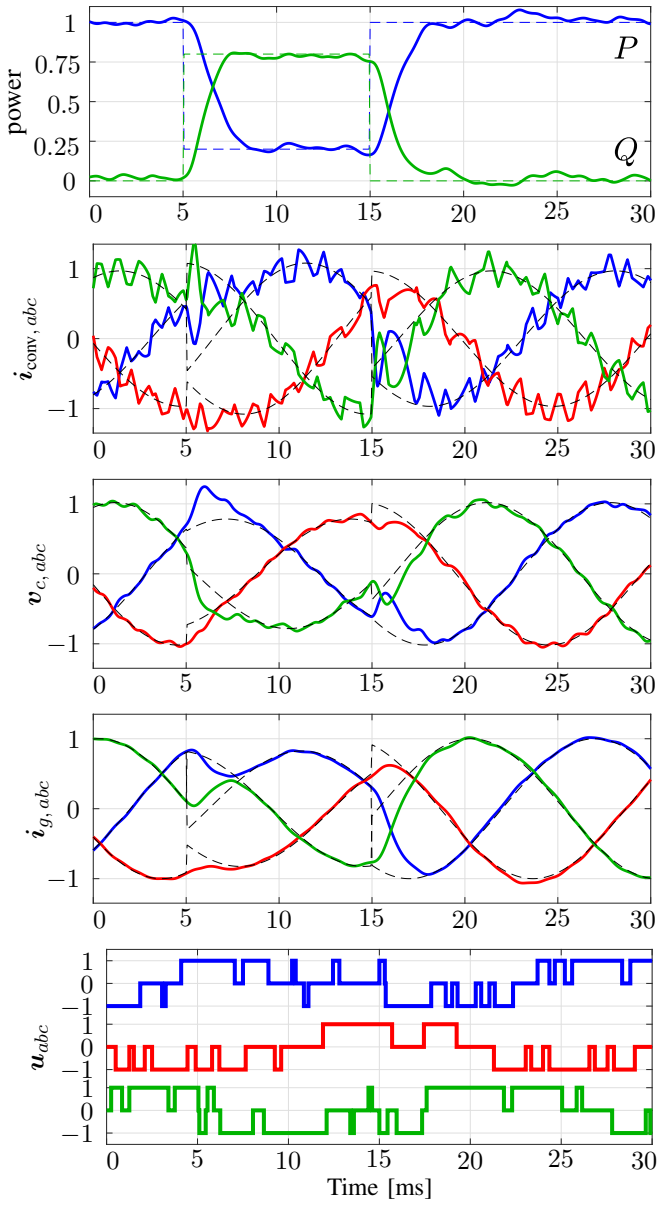

Fig. 7. Simulation results at transient operation with the proposed FCS-MPC for $N = \{4, 1\}$ when a mismatch of -50% is introduced in the grid reactance X_g and the estimator is active.

in Section III-B, while the value of λ_u is chosen to maintain $f_{\text{sw}} \approx 245\,\text{Hz}$. The prediction model (3) is updated at every sampling interval with the calculated value of the lumped grid-side reactance $\widehat{X}_\Sigma$, i.e., the scheme works in the presence of the -50% mismatch in X_g that is compensated for by the estimator.

The controller clearly demonstrates the ability to track all the references, thanks to its MIMO nature, while the grid current THD is $I_{g,\text{THD}} \approx 3.6\%$. The grid current harmonics do not violate the IEEE 519 standard [18], but they are spread over a wide range of frequencies, something typical for direct control methods. Moreover, as it can be observed, the most pronounced harmonics are concentrated at low frequencies, with the 7^{th} and 11^{th} being the most pronounced ones.

The transient operation of the scheme during power steps is examined in Fig. 7. At 5 ms, P_{ref} is changed from 1 to 0.2 p.u., and Q_{ref} is changed from 0 to 0.8 p.u. At 15 ms, the power levels return to their initial values. The controlled variables $\boldsymbol{y}$ accurately follow their references $\boldsymbol{y}_{\text{ref}}$ with very short settling times, which are below 4 ms. Such behavior is typical for direct control methods, as

they can exploit all the available voltage margin when minimizing the tracking error.

VII. Conclusion

This paper proposed a long-horizon FCS-MPC algorithm tailored for MV grid-tied three-level NPC converters with LCL filters. The scheme comes with a reduced calculation load and an effective, yet simple, estimation algorithm to account for mismatches in the grid reactance. The presented results show superior steady-state performance for the chosen range of switching frequencies as compared to the conventional one-step FCS-MPC. Moreover, the presented time domain results demonstrated the favorable multi-output tracking ability of the control scheme both for steady-state and transient operation.

Appendix

Coefficients in (12) are defined as

$$\begin{aligned}
A &= \Delta A_{g,\alpha}^2(k+1) + \Delta A_{g,\beta}^2(k+1) \\
&\quad - \Delta A_{g,\alpha}^2(k) - \Delta A_{g,\beta}^2(k)\,, \qquad (14a)\\
B &= 2\cdot(\Delta A_{g,\alpha}(k+1) v_{\text{conv},\alpha}(k) \\
&\quad + \Delta A_{g,\beta}(k+1) v_{\text{conv},\beta}(k) - \Delta A_{g,\alpha}(k) v_{\text{conv},\alpha}(k-1) \\
&\quad - \Delta A_{g,\beta}(k) v_{\text{conv},\beta}(k-1) \\
&\quad + X_{fc}\cdot(\Delta A_{g,\alpha}(k+1)\Delta A_{\text{conv},\alpha}(k+1) \\
&\qquad + \Delta A_{g,\beta}(k+1)\Delta A_{\text{conv},\beta}(k+1) \\
&\qquad - \Delta A_{g,\alpha}(k)\Delta A_{\text{conv},\alpha}(k) \\
&\qquad - \Delta A_{g,\beta}(k)\Delta A_{\text{conv},\beta}(k))\,, \qquad (14b)\\
C &= v_{\text{conv},\alpha}^2(k) + v_{\text{conv},\beta}^2(k) \\
&\quad - v_{\text{conv},\alpha}^2(k-1) - v_{\text{conv},\beta}^2(k-1) \\
&\quad + 2X_{fc}\cdot(\Delta A_{\text{conv},\alpha}(k) v_{\text{conv},\alpha}(k) + \Delta A_{\text{conv},\beta}(k) v_{\text{conv},\beta}(k) \\
&\qquad - \Delta A_{\text{conv},\alpha}(k-1) v_{\text{conv},\alpha}(k-1) \\
&\qquad - \Delta A_{\text{conv},\beta}(k-1) v_{\text{conv},\beta}(k-1))\\
&\quad + X_{fc}^2\cdot(\Delta A_{\text{conv},\alpha}^2(k+1) + \Delta A_{\text{conv},\beta}^2(k+1) \\
&\qquad - \Delta A_{\text{conv},\alpha}^2(k) - \Delta A_{\text{conv},\beta}^2(k))\,. \qquad (14c)
\end{aligned}$$

References

[1] P. Karamanakos, E. Liegmann, T. Geyer, and R. Kennel, "Model predictive control of power electronic systems: Methods, results, and challenges," *IEEE Open J. Ind. Applicat.*, vol. 1, pp. 95–114, Aug. 2020.

[2] T. Geyer, *Model Predictive Control of High Power Converters and Industrial Drives*. Hoboken, NJ, USA: Wiley, 2016.

[3] P. Karamanakos and T. Geyer, "Guidelines for the design of finite control set model predictive controllers," *IEEE Trans. Power Electron.*, vol. 35, no. 7, pp. 7434–7450, Jul. 2020.

[4] T. Geyer and D. E. Quevedo, "Multistep finite control set model predictive control for power electronics," *IEEE Trans. Power Electron.*, vol. 29, no. 12, pp. 6836–6846, Dec. 2014.

[5] P. Karamanakos, T. Geyer, and R. Kennel, "A computationally efficient model predictive control strategy for linear systems with integer inputs," *IEEE Trans. Contr. Syst. Technol.*, vol. 24, no. 4, pp. 1463–1471, Jul. 2016.

[6] P. Karamanakos, T. Geyer, N. Oikonomou, F. D. Kieferndorf, and S. Manias, "Direct model predictive control: A review of strategies that achieve long prediction intervals for power electronics," *IEEE Ind. Electron. Mag.*, vol. 8, no. 1, pp. 32–43, Mar. 2014.

[7] S. Baltruweit, E. Liegmann, P. Karamanakos, and R. Kennel, "FPGA-implementation friendly long-horizon finite control set model predictive control for high-power electronic systems," in *Proc. IEEE Energy Convers. Congr. Expo. Asia*, Singapore, Singapore, May 2021, pp. 1823–1828.

[8] D. Zhou, H. Wang, and F. Blaabjerg, "Reactive power impacts on LCL filter capacitor lifetime and reliability in DFIG grid-connected inverter," in *Proc. IEEE Energy Convers. Congr. Expo.*, Portland, OR, USA, Sep. 2018, pp. 4094–4101.

[9] M. K. De Meerendre, E. Prieto-Araujo, K. H. Ahmed, O. Gomis-Bellmunt, L. Xu, and A. Egea-Alvarez, "Review of local network impedance estimation techniques," *IEEE Access*, vol. 8, pp. 213 647–213 661, Nov. 2020.

[10] N. Hoffmann and F. W. Fuchs, "Minimal invasive equivalent grid impedance estimation in inductive–resistive power networks using extended Kalman filter," *IEEE Trans. Power Electron.*, vol. 29, no. 2, pp. 631–641, Feb. 2014.

[11] A. Malkhandi, N. Senroy, and S. Mishra, "A dynamic model of impedance for online Thevenin's equivalent estimation," *IEEE Trans. Circuits Syst. II*, vol. 69, no. 1, pp. 194–198, Jan. 2022.

[12] Y. Cheng, W. Wu, H. Chung, F. Blaabjerg, K. Eftychios, and L. Zhu, "Using Kalman filter to achieve online estimation of equivalent grid impedance and high bandwidth control for LCL-filtered grid-tied inverters," in *Proc. IEEE Ind. Electron. Conf.*, Singapore, Singapore, Oct. 2020, pp. 4247–4252.

[13] S. Cobreces, E. Bueno, D. Pizarro, F. Rodriguez, and F. Huerta, "Grid impedance monitoring system for distributed power generation electronic interfaces," *IEEE Trans. Instrum. Meas.*, vol. 58, no. 9, pp. 3112–3121, Sep. 2009.

[14] D. Perez-Estevez and J. Doval-Gandoy, "Grid impedance identification using the VSC switching ripple," in *Proc. IEEE Energy Convers. Congr. Expo.*, Baltimore, MD, USA, Sep. 2019, pp. 1506–1513.

[15] A. Tregubov, P. Karamanakos, and L. Ortombina, "Long-horizon robust direct model predictive control for medium-voltage induction motor drives with reduced computational complexity," *IEEE Trans. Ind. Appl.*, vol. 59, no. 2, pp. 1775–1787, Mar./Apr. 2023.

[16] E. Liegmann, P. Karamanakos, and R. Kennel, "Real-time implementation of long-horizon direct model predictive control on an embedded system," *IEEE Open J. Ind. Appl.*, vol. 3, pp. 1–12, 2022.

[17] B. Arif, L. Tarisciotti, P. Zanchetta, J. C. Clare, and M. Degano, "Grid parameter estimation using model predictive direct power control," *IEEE Trans. Ind. Appl.*, vol. 51, no. 6, pp. 4614–4622, Nov./Dec. 2015.

[18] *IEEE Standard for Harmon. Control in Elect. Power Syst.* IEEE Std 519-2022, 2022.